Cation Distribution and Coordination Chemistry of Cu(II) in Zn(II) Hydroxide Nitrate Solid Solutions: A Structural and Spectroscopic Study

M. Atanasov, K. Petrov, and E. Mirtcheva

Institute of General and Inorganic Chemistry, Bulgarian Academy of Sciences, 1113-Sofia, Bulgaria

and

C. Friebel and D. Reinen

Fachbereich Chemie und Zentrum für Materialwissenschaften der Philipps-Universität, Hans-Meerwein-Strasse, D-35032 Marburg, Germany

The X-ray powder diffraction analysis of the appearing phases in hydroxide nitrate compounds (Zn_xCu_{1-x}) $(OH)_{2-y}(NO_3H)_y \cdot zH_2O$ is reported. Single-phase solid solutions are detected only for $0 < x < 0.30$ (structural type $Cu_2(OH)_3NO_3$, phase I) and for $0.50 < x < 0.65$ (structural type $Zn_3(OH)_4(NO_3)_2$, phase I'). In the interval $0.3 < x < 0.5$ the structurally closely related phases I and I' coexist. For $0.65 < x \leq 1.0$ a second two-phase region with I' and a third structure type $Zn_5(OH)_8(NO_3)_2 \cdot 2H_2O$ (phase II-b) was observed. From the intensities of the X-ray reflections and the dependence of the lattice parameter b' on x it was deduced that only a small fraction of Cu^{2+} enters phase II-b. Using the structural data and the EPR spectra together with calculations within the angular overlap model (AOM) the observed EPR signals could be correlated with the occupation of the various Zn^{2+} sites by Cu^{2+} in the three phases. It was also possible to derive the changes of the Zn^{2+} host site geometries induced by substituting Cu^{2+} ions due to vibronic coupling. The nicely resolved EPR spectra at high x values originate from small amounts of Cu^{2+} in phase II-b. They display patterns of tetragonally elongated and—in the dynamical average—compressed $Cu(OH)_6$ octahedra at higher temperatures, which are assigned to the Zn(2) and Zn(1) sites, respectively. At 5 K the latter polyhedron freezes into a geometry with a strong orthorhombic distortion component due to vibronic Jahn—Teller coupling. The EPR spectra further indicate that the bulk of Cu^{2+} enters phases I and I'. Powder reflectance spectra at 5 K are in support of these conclusions. The bonding parameters of Cu^{2+} in phase II-b have been determined from the well-resolved hyperfine structure in the EPR spectra. © 1995 Academic Press, Inc.

I. INTRODUCTION

Layered hydroxide nitrates of transition metals have been studied extensively because of their use as precursors for the synthesis of simple and complex metal oxides with interesting magnetic, conducting, and catalytic properties. The recent development of a method for preparing solid solutions of hydroxide nitrates of different metal ions with controlled composition (1) offered the possibility of studying the substitution of closed-shell ions by magnetic ones and to connect the geometry of the occupied sites with the electronic configuration of the magnetic ions. Especially Cu(II) (d^9) in a pseudo-octahedral coordination of OH^- and NO_3^- ligands was studied and characterized with respect to its electronic structure and environmental geometry by combined use of X-ray diffraction and spectroscopic (ESR, optical) methods (2). We could show that in a $Mg_2(OH)_3NO_3$ host lattice with two different pseudo-octahedral sites [one *trans*-$Mg(OH)_4(NO_3)_2$ (site 1) and one $Mg(OH)_5NO_3$ (site 2)] Cu(II) preferentially enters the more distorted site 1 following its natural tendency to gain energy via polyhedral distortions of the Jahn–Teller type. In the course of extending these studies to analogous compounds of the formal composition $(Zn_xCu_{1-x})(OH)_{2-y}(NO_3)_y \cdot zH_2O$ ($O \leq x \leq 1.0$) we obtained results regarding the appearance of various phases with layer structures, on the one hand, and the distribution of Cu(II) substituting Zn(II) over different sites, on the other.

II. EXPERIMENTAL

1. Sample Preparation

Thirteen samples of zinc–copper hydroxide nitrates with the formal composition $(Zn_xCu_{1-x})(OH)_{2-y}(NO_3)_y \cdot zH_2O$ ($0 \leq x \leq 1.0$, $0.4 \leq y \leq 0.67$, $0 \leq z \leq 0.4$)—x, y, and z being independent parameters—were prepared by the double-jet precipitation method (1, 2). Equal amounts of 0.5 M sodium hydroxide and copper(II) nitrate solutions were added simultaneously at the same rate to

a preset quantity of 3.5 M Zn(II) nitrate solution stirred continuously. The rate of addition was adjusted experimentally to match the rate of evaporation, so that the volume of the suspension was maintained constant during the precipitation. The procedure ended when 75 at. % of the total content of the divalent ions were precipitated. In order to obtain different Zn to Cu atomic ratios in the solid products, the concentration of the $Cu(NO_3)_2$ solutions used for different samples varied between 0.0 and 0.5 M. The solid phases were filtered from the mother solutions, washed with water and ethanol, and dried at 60°C. All samples were polycrystalline powders whose color changed gradually from green-blue to light-blue and finally to white, with increasing Zn content.

2. Chemical Analysis

The total content of the divalent cations was determined using a combination of routine complexometric methods. The copper content was determined iodometrically.

3. X-Ray Diffraction (XRD) Analyses

XRD measurements were carried out using a powder diffractometer (Co$K\alpha$ radiation, Fe filter, scintillation counter, continuous chart recording of the diffraction pattern). A scanning speed of 1° (2θ) min^{-1} was used for the routine identification measurements. The refined values of the unit cell parameters were calculated from diffractograms recorded at a speed of (1/4)°(2θ) min^{-1}.

4. Diffuse Reflectance and EPR Spectra

The diffuse reflectance spectra were recorded on a Perkin–Elmer 330 UV-VIS-NEAR-IR spectrometer at room temperature and on a Zeiss PMQII Spectrometer (Infrasil) at 295 and 5 K. Freshly sintered MgO [8000–30000 cm^{-1}] was used as a standard. The reflectance data were converted into absorption values log(k/s) following the theory of Schuster–Kubelka–Munk (3).

EPR spectra at room temperature and at $\approx$130 K were taken with both a Varian (35 GHz, Q-band) and a Bruker X-band spectrometer. DPPH ($g = 2.0037$) was used as an internal standard.

5. Angular Overlap Calculations

Transition energies and g-tensor components were calculated within the angular overlap model (AOM) using the computer program AOMX (4). In the AOM calculations we used the exact geometry of the Zn(II) polyhedra as input data. Reference values of e_σ and e_π, the energy parameters describing the σ and π antibonding effects connected with the d contributions to the Cu–OH bonds, have been based on published data (5) from the optical

spectra of $Ba_2[Cu(OH)_6]$. They are $e_\sigma = 3600$ cm^{-1} and $e_\pi = 700$ cm^{-1} for a Cu–OH spacing of 2.10 Å.

In order to account for variations in the metal–ligand distance we used the relation

$$e_\lambda/e_\lambda' = S_\lambda^2/S_\lambda'^2 \quad (\lambda = \sigma, \pi), \quad [1]$$

where the S_λ are overlap integrals for the Cu–O bond, calculated using the program in (6).

III. RESULTS AND DISCUSSION

1. Structural Data

Three phases were observed within the partly inhomogeneous solids of the formal composition $(Zn_xCu_{1-x})(OH)_{2-y}(NO_3)_y \cdot zH_2O$, whose relative content and unit cell parameters vary systematically with x (Fig. 1). These phases, for the sake of convenience, will be denoted hereafter as I, I', II-b and are crystallographically specified in Table 1. The notation is in accordance with the classification of the structure types of the hydroxide nitrates of nickel and zinc, offered by Louër et al. (7).
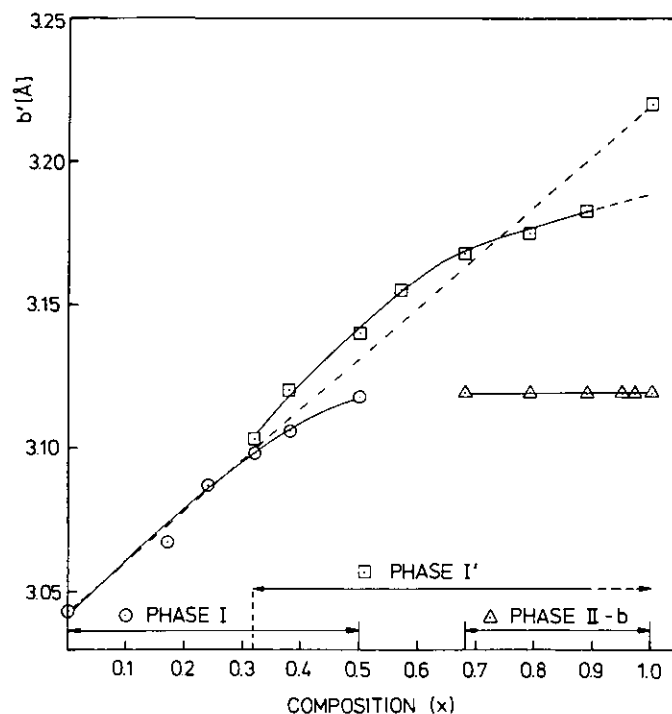

FIG. 1. Phase diagram of solids $(Zn_xCu_{1-x})(OH)_{2-y}(NO_3)_y \cdot zH_2O$ and the dependence of the b' unit cell parameter (Table 1) on x. The b' of $Zn_3(OH)_4(NO_3)_2$ is also indicated, illustrating that the unit cell parameters of the brucite-type compounds (phases I, I') depend approximately linearly on the Cu^{2+} concentration. (In the two-phase regions $(1 - x)$ is the average Cu^{2+} content in the respective two phases, weighted by the relative volume percentage, with which they occur in the mixture.)

TABLE 1
Structural Characteristics of $Cu_2(OH)_3NO_3(I)$, $Zn_3(OH)_4(NO_3)_2(I')$, and
$Zn_5(OH)_8(NO_3)_2 \cdot 2H_2O$ (II-b)

	$Cu_2(OH)_3NO_3$	$Zn_3(OH)_4(NO_3)_2$	$Zn_5(OH)_8(NO_3)_2 \cdot 2H_2O$
a [Å]	5.605	7.038[a]	19.48[a]
b [Å]	6.087	9.658	6.238
c [Å]	6.929[a]	11.182	5.517
β[°]	94.48	100.96	93.28
Space group	$P2_1$	$P2_1/c$	$C2/m$
Ref.	(8)	(9)	(10)
a' [Å]	5.605 = a	5.591 = $c/2$	5.517 = c
b' [Å]	3.044 = $b/2$	3.219 = $b/3$	3.119 = $b/2$
$\delta(\%)^b$	5.93	0.25	2.08

[a] Direction approximately perpendicular to the layers ($= c'$ and $= 3c'$, respectively).
[b] $\delta(\%) = [(a' - b'\sqrt{3})/a'] \times 100$.

At the experimental conditions used the sample with $x = 0$ is single-phase $Cu_2(OH)_3NO_3$ (phase I). Its crystal structure can be derived from that of brucite $Mg(OH)_2$, with the NO_3^- ions substituting 1/4 of the OH^- groups. The tetragonally distorted edge-sharing copper octahedra form pseudo-hexagonal $^2_\infty[Cu_2(OH)_3ONO_2]$ sheets approximately perpendicular to the $\langle 001 \rangle$ direction. Adjacent sheets are linked by hydrogen bonds. Cu^{2+} occupies two independent sites. Cu(1) is coordinated by four equatorial OH^- ions, at an average distance of 1.96_5 Å, and two axial oxygen atoms, belonging to NO_3^- groups at about 2.40 Å. Cu(2) is coordinated by four equatorial OH^- ligands at an average distance of 1.99_5 Å and in the axial directions by one OH^- and one NO_3^- group at 2.31 Å and 2.39 Å, respectively; it is hence less distorted than the Cu(1) polyhedron (8).

With increasing Zn content the system remains single phase. At $0.3 < x < 0.6$, however, reflections of a second phase, I', appear additionally in the diffraction patterns. Its prototype is zinc hydroxide nitrate, $Zn_3(OH)_4(NO_3)_2$, the structure of which (9) is topologically similar to that of $Cu_2(OH)_3NO_3$, containing sheets of almost hexagonally packed edge-sharing $Zn(OH)_4(NO_3)_2$ octahedra approximately perpendicular to the $\langle 100 \rangle$ direction linked by hydrogen bonds, similar to $Cu_2(OH)_3NO_3$. Three independent sites are present, Zn(1) and Zn(2) being coordinated by four OH^- ions and two "cis" oxygen atoms belonging to NO_3^- groups, while Zn(3) is surrounded by four equatorial OH^- ligands and two "trans" oxygen atoms of nitrate ions (Fig. 2). The three $[Zn(OH)_4(ONO_2)_2]^{2+}$ octahedra are considerably distorted even if the large standard deviations of the geometrical parameters are taken into account. The unit cell of $Zn_3(OH)_4(NO_3)_2$ is actually a supercell of the $Cu_2(OH)_3NO_3$ cell, due to the specific ordering of the $Zn_3(OH)_4(NO_3)_2$ polyhedra. Between $x \approx 0.55$ and $x \approx 0.65$ only reflections due to phase I' are observed (Fig. 1).

At $x \approx 0.65$ the diffraction pattern of phase I' looses intensity with increasing x, vanishing at $x = 1.0$. In the same interval of x reflections of a third phase, II-b, the prototype for which is $Zn_5(OH)_8(NO_3)_2 \cdot 2H_2O$ (10), appear. The latter structure can also be derived from the brucite structure, removing 1/4 of the metal cations and blocking opposite triangular faces of the respective unoccupied octahedra by tetrahedrally coordinated Zn^{2+} ions. It contains three independent Zn^{2+} ions (Fig. 3). Zn(1) is coordinated by four equatorial OH^- ions at a distance of 2.19 Å and two axial OH^- ions at 2.02 Å. Zn(2) is surrounded by two axial OH^- ions at a distance of 2.16 Å, and two cis pairs of equatorial OH^{-1} ions at distances of
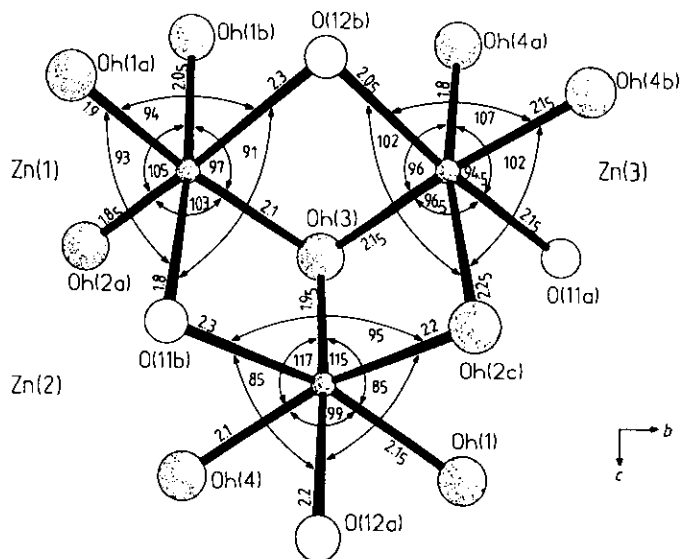

FIG. 2. The Zn^{2+} coordination geometries in $Zn_3(OH)_4(NO_3)_2$. (Experimental standard deviations are between $\pm 0.04_5$ Å and $\pm 0.02_5$ Å and $\pm 1.2°$ for the Zn–O spacings and the O–Zn–O bond angles, respectively).
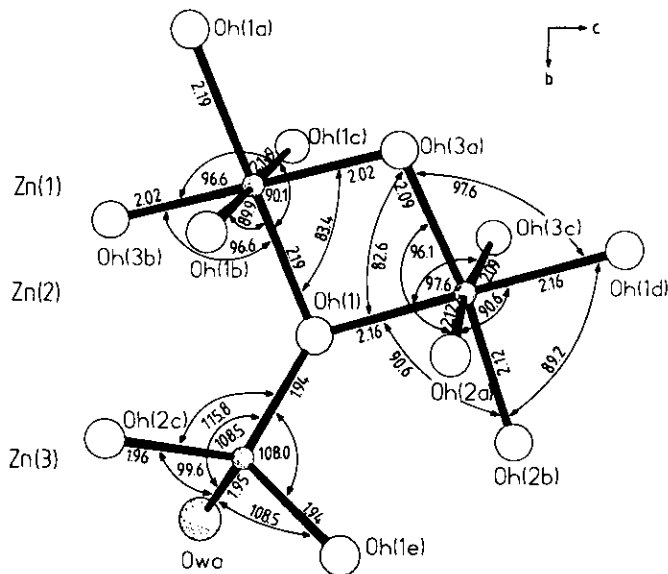
FIG. 3. The Zn^{2+} coordination geometries in $Zn_5(OH)_8(NO_3)_2$. (Experimental standard deviations are ± 0.006 Å and $\pm 0.02_5°$ for the Zn–O spacings and the O–Zn–O bond angles, respectively.)

2.12 and 2.09 Å, respectively, which exhibit large angular distortions and considerable ($\approx \pm 0.125$ Å) tetrahedral-type deviations from the equatorial plane (Fig. 3). Zn(3) is pseudo-tetrahedrally coordinated by two OH⁻ ions at 1.94 Å, one OH⁻ ion at 1.96 Å, and one water molecule at 1.95 Å, with rather large angular distortions. The oxygen atoms of the NO_3^- anions are not bonded to the metal ions, and in contrast to the type I and I' phases, they are located between the charged sheets, linking them together. Surprisingly the two different $Zn(OH)_6^{4-}$ octahedra are strongly distorted, though all ligands are identical. We think that the cationic coordination of the OH⁻ ions is informative in this respect. The ligator atoms Oh(1) and Oh(2) in Fig. 3 are bonded to one "tetrahedral" and two "octahedral" Zn^{2+} ions. Contrapolarizing effects induced by the short Zn(3)–O spacings (≈ 1.95 Å) apparently lead to rather long Oh(1, 2)–Zn(1, 2) distances between 2.19 and 2.12 Å. On the other hand, Oh(3) is coordinated to three "octahedral" Zn^{2+} ions which leads to shorter Zn(1, 2)–Oh(3) bonds between 2.02 and 2.09 Å.

The data in Table 1 shows that the parameter b' should be the quantity which is the most sensitive to distinguish between the structurally closely related phases I and I', when varying x. The results of the refinements of the lattice parameters for I, I' proved this assumption, showing also that the dependencies of a', c', and β on the composition are small or not informative in the context of this paper.

One may ask how large the relative volume fractions of each phase are in the two-phase regions. The overlap

of the strongest XRD reflections in the interval of coexistence of phases I and I' does not allow a precise quantitative analysis to be performed. Such analysis, however, was possible in the region where phases I' and II-b coexist. It shows that the relative volume fraction of phase I' decreases almost linearly from 100% ($x = 0.6$), to 8% ($x = 0.96$). Assuming further that b' of phase I' varies linearly with the Cu^{2+} concentration it follows that only about 2 to 5% of the total copper amount substitutes Zn^{2+} in the II-b host lattice, in agreement with the observation that the unit-cell parameters of II-b do not change significantly.

We may conclude by stating that the compositional parameter x in Fig. 1 correlates with the true Cu^{2+} concentration at $x < 0.3$ [$Zn_{2x}Cu_{2-2x}(OH)_3NO_3$ (type I)] and in the region $0.5 < x < 0.6_5$ [$Zn_{3x}Cu_{3-3x}(OH)_4(NO_3)_2$ (type I')], while it is a weighted average over type I and type I' mixed crystals in the two-phase region $0.3 \lesssim x \lesssim 0.5$. In the two-phase region $x \gtrsim 0.65$ finally mixed crystals of type I' and the compound $Zn_5(OH)_8(NO_3)_2 \cdot 2$ H_2O—containing only a very small percentage of the total amount of Cu^{2+}—coexist and x again represents a weighted average compositional parameter.

2. Analysis of the EPR Spectra

In the following we make use of the Cu(II) EPR spectrum as a probe characterizing the various sites in the three phases that appear. We will use the structural data together with calculations within the AOM to correlate the observed EPR signals with the geometries of the Zn^{2+} host octahedra. This information together with the phase diagram (Fig. 1) will also give insight concerning the distribution of Cu(II) and its preference to enter the various sites.

EPR signals were only observed in the concentration region $0.4 \lesssim x < 1.0$. In the Q-band spectra taken at 100 K well-resolved signals were observed, the positions of which are not concentration dependent and which are used to deduce the g- and A-tensor components at this temperature (Table 2, Fig. 4). The EPR spectrum of the mixed crystal with $x = 79$ for example shows five signals of dominant intensity, four of which exhibit fine structure due to the coupling of the unpaired electron with the $I = 3/2$ nuclear moment of Cu^{2+}. We can group these signals into pairs belonging to two Cu^{2+} sites which we denote P1 and P2 in the following. Spectrum P2 with $g_\perp \simeq 2.08$ and $g_\| = \simeq 2.41$ corresponds apparently to an elongated octahedron (see Eq. [2]). A compressed tetrahedron would induce a similar g tensor, but such a geometry is not present in phases I' and II-b, however, as evidenced by the structural data and AOM calculations (vide infra). Spectrum P1 with $\bar{g}'_\perp \simeq 2.29$ and $\bar{g}'_\| \simeq 2.01_5$ is typical for

TABLE 2

A and g Tensor Components, Line Width Values W, and Relative P1 and P2 Occupancies in Solids with the Formal Composition $Zn_xCu_{1-x}(OH)_{2-y}(NO_3)_y \cdot zH_2O$, Used for Spectral Simulations (Fig. 4)

x	T [K]	ν [GHz]	Species relative amount[a]		g_x	g_y	g_z	g_{av}	$|A_x|$	$|A_y|$	$|A_z|$ [10^{-4} cm^{-1}]	w_x	w_y [Gauss]	w_z
0.96₅	130	35.342	P2	0.93	2.078	2.080	2.409	2.189	0	0	124	10	9	6
			P1	0.07	2.297	2.271	2.015	2.194	38	47	84	10	10	7
0.79	100	33.970	P2	0.93	2.078	2.080	2.413	2.190	0	0	123	10	10	8
			P1	0.07	2.302	2.275	2.016	2.198	36	49	84	10	10	8
	4	33.976	P2	0.95	2.075	. 2.079	2.411	2.188	0	0	126	11	11	15
			P1	0.05	2.397	2.168	2.020	2.195	83	0	71	12	24	12

Note. The g and A values of site P1 are denoted by g_i', A_i', and $\overline{g}_i'$, $\overline{A}_i'$ ($i = x, y, z$) in the text for the statically distorted (low temperature) and dynamically averaged geometry (high temperature), respectively.

[a] Corresponding to the superposition of first-derivative spectra.

Cu^{2+} in tetragonally compressed octahedra [d_z^2 – ground state; see Eq. (3)], though a distinct orbital contribution to $\overline{g}_\parallel'$ is present (see below). The $\overline{g}_\perp'$ signal is slightly split due to a small orthorhombic ligand field component. The hyperfine splitting of each P1 signal is nicely resolved (Table 2).

We will base the analysis of the g- and A-tensor compo-

nents on a tetragonal geometry first and refine the results by explicitly taking into account lower-symmetry components subsequently. The following expressions for the g and A values of Cu^{2+} in an elongated (compressed) octahedral coordination of D_{4h} symmetry [$d_{x^2-y^2}(d_{z^2})$ ground state] allow the deduction of information about the geometry of and the bonding in the CuO$_6$ polyhedra;
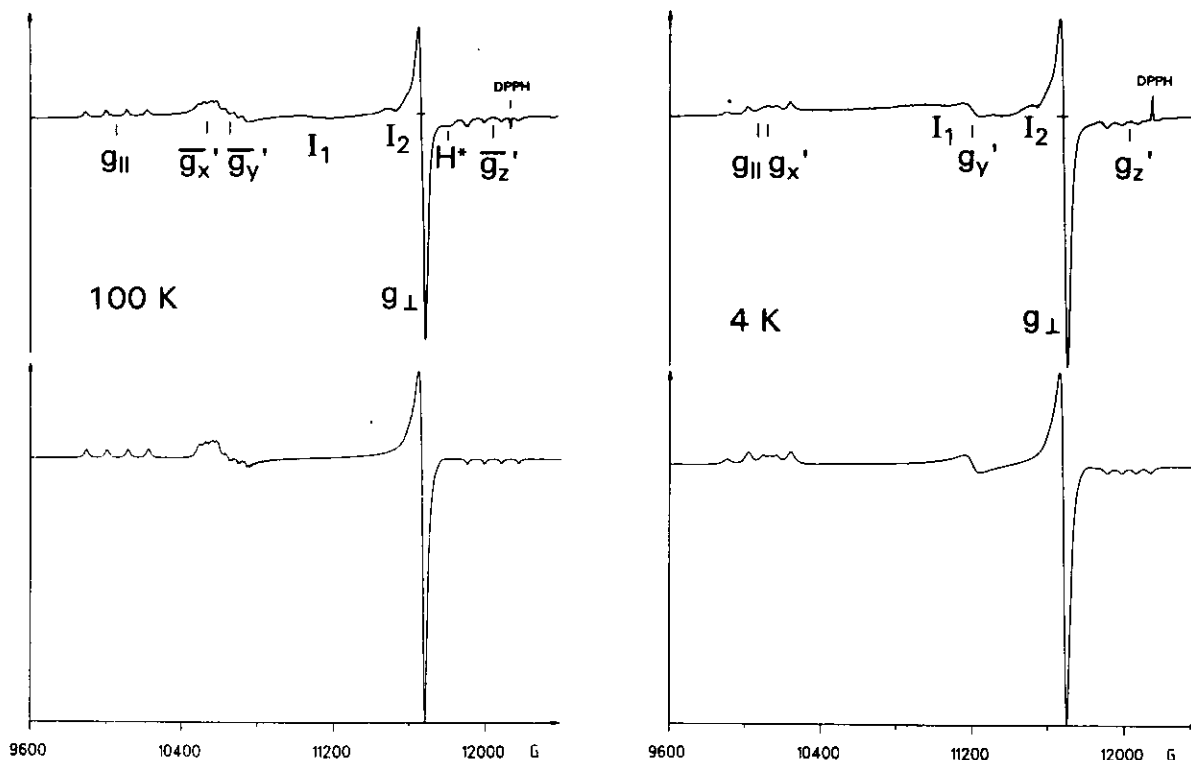

FIG. 4. Experimental EPR spectra (Q-band) of solids with the formal composition $Zn_xCu_{1-x}(OH)_{2-y}(NO_3)_y \cdot zH_2O$ ($x = 0.79$) at 100 K and 4 K (above) and simulations with the parameters listed in Table 2 (below). The three features I_1, I_2, and H* are discussed in the text.

ground state:

$$g_\parallel = g_0 + 8u_\parallel - 3u_\perp^2 - 4u_\parallel u_\perp \quad u_i = k_i^2 \zeta_0/\Delta_i \quad (i = \parallel, \perp)$$
$$g_\perp = g_0 + 2u_\perp - 4u_\parallel^2 \qquad\qquad \Delta_\parallel = E(^2B_2) - E(^2B_1),$$
$$\Delta_\perp = E(^2E) - E(^2B_1) \quad [2a]$$

$$A_\parallel = P[(-\kappa - 4/7)\alpha^2 + \Delta g_\parallel + (3/7)\Delta g_\perp] \quad [2b]$$
$$A_\perp = P[(-\kappa + 2/7)\alpha^2 + (11/14)\Delta g_\perp]$$

ground state:

$$\bar{g}'_\parallel = g_0 - 3u'^2_\perp \quad u'_\perp = k'^2_\perp\zeta_0/\Delta'_\perp \quad [3a]$$
$$g'_\perp = g_0 + 6u'_\perp - 6u'^2_\perp \quad \Delta'_\perp = E(^2E) - E(^2A_1)$$

$$A'_\parallel = P[(-\kappa' + 4/7)\alpha'^2 - (1/7)\Delta g'_\perp] \quad [3b]$$
$$A'_\perp = P[(-\kappa' - 2/7)\alpha'^2 + (15/14)\Delta g'_\perp],$$

Here k_i and $k'_i(i = \parallel, \perp)$ are the orbital reduction factors, the Δg are the deviations of the g values from g_0, and ζ_0 is the free ion spin–orbit coupling constant for Cu^{2+} ($\zeta_0 = 830$ cm^{-1}). The variables α and α' denote the mixing coefficients of the $[d_{x^2-y^2}(d_{z^2})]$ wave functions in the singly occupied ground state molecular orbital (MO)

$$\Psi_g[x^2 - y^2(z^2)] = \alpha(\alpha')d_{x^2-y^2}(d_{z^2}) - \delta(\delta')L_{x^2-y^2}(L_{z^2}), \quad [4]$$

where $L_{x^2-y^2}(L_{z^2})$ is the symmetry adapted linear combination of ligand orbitals. The scaling factor $P = g_e g_N \beta_e \beta_N \langle r^{-3}\rangle$ has been estimated as 360×10^{-4} cm^{-1} for Cu^{2+} (11, 12), and κ is the Fermi contact term with a value 0.43 for the free ion Cu^{2+} $3d$ orbitals. The hyperfine tensor components A may be either negative or positive, which has to be carefully checked in each case. $A_{\perp,\parallel}$ and $A'_\perp$ have to be taken with a negative sign in our case, in order to obtain meaningful α, α', and κ values.

The mean g values of the spectra P1 (2.19$_5$) and P2 (2.19) are close to each other, implying that the coordinating ligands of the two species are very similar, differing only slightly in the extent of polyhedron distortion (see below). From the hyperfine tensor components (Table 2, Eqs. [2, 3]) we calculate for the elongated octahedron (signal P2)—using $\kappa = 0.43$—$\alpha = 0.88_5$ and $A_\perp = -19 \times 10^{-4}$ cm^{-1}, which is too small to be resolved at Q-band frequencies. Even with a vanishing $A_\perp$ value we were able to simulate fairly well the X-band absorption profile in this region. Negative $A_\parallel$ and negative or vanishing $A_\perp$ values are indeed characteristic for elongated Cu^{2+} coordination octahedra (13).

In the case of the compressed geometry, where negative $\bar{A}'_\perp$ and positive $\bar{A}'_\parallel$ values have to be chosen, in order to obtain consistent results (Table 2), α' is calculated to

be 0.90, if κ' is taken as the second variables beside α'. While the value of the mixing coefficient is consistent with the one for P2 and the previous results for mixed crystals $Cu_xMg_{2-x}(OH)_3(NO_3)$ ($\alpha = 0.90$) (2), $\kappa' = 0.23$ is strongly reduced with respect to the value expected for a $3d$ ground state ($\kappa_{3d} = 0.43$). The observed negative contributions to κ' originate from a hybridization of $3d_{z^2}$ with $4s$, which possesses the same a_{1g} symmetry in a D_{4h} surrounding (13). The isotropic hyperfine constant κ_{4s} for the free Cu^{2+} ion is -5.56 (14), and hence a reduction of the magnitude of κ' with respect to κ_{3d} or even a negative value is expected. If the mixing coefficient γ of the $4s$ orbital in the ground state MO (Eq. [4]) is small with respect to α' we may estimate an approximate value using

$$\gamma^2 \cong \alpha'^2(\kappa' - \kappa_{3d})/\kappa_{4s}. \quad [5]$$

It is interesting to compare the obtained value $\gamma^2 = 0.03$ with corresponding coefficients of Cu^{2+} doped into Ba_2ZnF_6 and K_2ZnF_4 host lattices with compressed ZnF_6^{4-} polyhedra, for which similar values of 0.05 and 0.026, respectively, are reported (13).

Spectrum P1 changes drastically when lowering the temperature to 4 K. The g'_x and g'_y signals, which nearly coincide at 100 K (Fig. 4), separate from each other such that the g'_x hyperfine structure overlaps with the one of $g_\parallel$ from species P2, while the g'_y signal shifts to $\approx$2.17 with an unresolved hyperfine splitting (Fig. 4), which can be estimated from the line width to be <15 $\times$ 10^{-4} cm^{-1}, however. Apparently the compressed geometry observed at higher temperatures is dynamically averaged, the underlying static distortion being strongly orthorhombic. We will discuss this feature in more detail below. The EPR spectra at high and low temperatures (Fig. 4) could be simulated rather nicely with the parameter set listed in Table 2.

3. Assignment of EPR Spectra to Specific Zn^{2+} Sites

The following experimental findings are of importance in assigning the EPR signals to the Zn^{2+} sites in the three phases:

(a) The EPR spectra observed in the region $1.0 > x > 0.6$ can only be due to Cu^{2+} in phases I' and II-b (Fig. 1).

(b) The analysis of the X-ray diffraction data shows that phase I' contains a rather high Cu^{2+} concentration, while in phase II-b only a small percentage of Cu^{2+} is present (Section III.1).

In order to assign the characterized P1 and P2 spectra to two of the possible six crystallographic sites in phases I' and II-b, we performed calculations within the AOM using as input the exact geometry of the Zn(II) polyhedra from the structural data and not accounting for the fact that Cu^{2+} can modify the host site geometry by vibronic

Jahn–Teller coupling. In these calculations we used rough estimates for the σ- and π-antibonding Cu–OH e_σ and e_π parameters, characterizing the bonds (see Section II.5). The calculations for I′ yielded g-tensor components which are strongly orthorhombic in accordance with the considerably distorted geometries of the ZnO_6 polyhedra (Fig. 2). This is not in agreement with the observed spectra P1, P2 at higher temperatures, which are expected to reflect the symmetry of the Zn^{2+} host polyhedra (though the extent of distortion should be considerably larger—see below). This is so because vibronic coupling effects of the Jahn–Teller type are of a dynamic nature, and thus do not break the site symmetry. The calculated g values for the two octahedral sites Zn(1) and Zn(2) and the tetrahedral site Zn(3) of phase II-b are found in Table 3.

A Cu^{2+} cation entering the Zn(1) site should possess a d_{z^2} ground state connected with the strongly compressed host site geometry (Fig. 3), if vibronic coupling is not taken into account (see the calculated g values and electronic transition energies in Table 3). The ground state of Cu^{2+} adopting the Zn(2) site geometry is apparently $d_{x^2-y^2}$ with a practically tetragonal g tensor and a term sequence, which both are in accordance with a tetragonally elongated octahedron (Table 3). This is very surprising considering the strongly distorted host-site geometry (Fig. 3) at first sight, but finds its explanation in the tensor properties of g, which cannot distinguish between differing spacings and bond angles of ligands in *trans* position. A closer look at the calculated transition energies shows a small low-symmetry splitting, but apparently the deviation from tetragonality is not large enough to influence the g factors significantly. The effective elongated D_{4h} geometry of position (2) indeed nicely matches with spectrum P2. We then assign spectrum P1 to the compressed Zn(1) site, because Cu^{2+} on the distorted tetrahedral site Zn(3) should have a strongly orthorhombic g tensor with widely varying g values (Table 3) even at high temperatures, which is not observed. The assignment of

the discussed main features in the EPR spectra to Cu^{2+} in phase II-b is confirmed by the observation of a hyperfine structure, which is indeed in accord with the high dilution of Cu^{2+} in this host compound.

The temperature dependence of spectrum P1 is exactly the one expected for Cu^{2+} doped into a site which is tetragonally compressed due to packing and bonding effects in the host structure (see Section III.1). Vibronic coupling of the Jahn–Teller type tends in such a case—besides usually enhancing the extent of distortion (increase of radial distortion parameter, see Eq. [6])—to transform the compression into an elongation (15). The latter geometry is preferred by Cu^{2+} as the consequence of higher order vibronic interactions. The energetic compromise between Jahn–Teller coupling and strain influence is the orthorhombic geometry, as manifested by the g-tensor anisotropy observed at 4 K. The polyhedron energetically stabilizes by increasing the Zn(1)–Oh(1), (1a) spacings and by decreasing the Zn(1)–Oh(1b), (1c) bond lengths or vice versa (Fig. 3). At higher temperatures the two mentioned conformations dynamically equilibrate, having an approximately compressed octahedron as their time average. One prominent example of this kind is the "$CuCl_4(OH)_2$" center in NH_4Cl, which has been studied and analyzed by EPR single crystal measurements (16). The small orthorhombic component of the g tensor at 100 K is most probably caused by a tiny bonding anisotropy in the Zn(1)Oh(1) Oh(1a) Oh(1b)Oh(1c) plane of the $Zn(1)O_6$ host octahedron (Fig. 3), not revealed by the structure analysis.

Looking at the calculated tensor components in Table 3 the average g value ($\approx 2.20_7$) connected with Zn(1) nearly equals the experimental one ($\approx 2.19_5$; Table 2). Apparently, the additional vibronic Jahn–Teller coupling is such that it only slightly enhances the local distortion but mainly modifies the site symmetry as outlined above. Apparently the lattice frame is rather stiff, presumably caused by the extensive polyhedron interconnection, thus

TABLE 3

Calculated g Values and Term Energies for Cu^{2+} at the Zn Sites of the $Zn_5(OH)_8(NO_3)_2 \cdot 2H_2O$ (Phase II-b) Host Structure[a]

Chromophore	g_x	g_y	g_z	d–d Transition energies			Ground state
				$(B_{1g}; x^2\text{-}y^2)$	$(E_g; yz, xz)$	$(B_{2g}; xy)$	
Zn(1)(OH)$_6$	2.315	2.315	1.989	4615 $(A_{1g}; z^2)$	8875, 9070 $(B_{2g}; xy)$	10324 $(E_g; xz, yz)$	$A_{1g}(z^2)$
Zn(2)(OH)$_6$	2.109	2.109	2.501	2000	7649	7829, 8065	$B_{1g}(x^2\text{-}y^2)$
Zn(3)(OH)$_3$H$_2$O[b]	3.422	1.182	2.210	327	1543 5527	6082	—

[a] The g-tensor components are calculated using $\zeta^{\text{eff}} = 500$ cm^{-1} ($k = 0.77_5$) which is in accord with the value deduced for Cu^{2+} in Ba_2Cu (OH)$_6$ and $Mg_2(OH)_3NO_3$ (2). LS coupling is not taken into account in calculating the term energies, in order to avoid revealing possible low-symmetry splittings.

[b] Band assignments are not given, because they are not relevant in the context of the paper.

preventing larger local distortions. We consider this argument, which to a lesser degree also holds for the Zn(2) site (vide infra), to explain why Cu^{2+} preferentially enters phase I'. Here—in spite of the structural similarity—the presence of oxygen ligator atoms from coordinating nitrate groups with rather weak metal-to-ligand bonds allows a much stronger Jahn–Teller distortion and hence a considerably larger ground state stabilization.

The deviations of the bond lengths δR_i $(i = x, y, z)$ from the mean value for a D_{2h} distorted octahedron are parametrized by the angular distortion parameter ϕ and the radial distortion parameter ρ (Eq. [6]). The values $\phi = 180°$, $300°$, and $60°$ and $\phi = 0°$, $120°$, and $240°$ describe the

$$\delta R_x = \rho \cos(\phi - 120°)/\sqrt{3} \quad \delta R_y = \rho \cos(\phi + 120°)/\sqrt{3}$$

$$\delta R_z = \rho \cos \phi/\sqrt{3} \qquad \rho = [2(\delta R_x^2 + \delta R_y^2 + \delta R_z^2)]^{1/2}$$

$$(6)$$

octahedra, compressed and elongated along z, x, and y, respectively. The ϕ values deviating from these angles specify polyhedra with orthorhombic geometries. Inserting the g_i' $(i = x, y, z)$ values for Cu^{2+} on the Zn(1) position at 4 K (Table 2) into the expressions for A_i' $(i = x, y, z)$ for a general orthorhombic geometry (see Appendix), ϕ, κ', and α' result as solutions of the corresponding set of nonlinear equations. The obtained values of $\kappa'(0.23)$ and $\alpha'(0.93_5)$ are more reliable than those at 100 K, because Eq. [3] is not strictly applicable to a system which is compressed only in the dynamical average, without possessing a pure d_z^2 ground state. The value of ϕ is calculated to be $\pm 26°$, nearly intermediate between a $d_{x^2-y^2}$ $(\phi = 0)$ and a d_z^2 (d_y^2) ground state $(\phi = \pm 60°)$. The radial distortion parameter for the Zn(1) host site (Fig. 3, Eq. [6]) is 0.25 Å, slightly smaller than the expected ρ value for Cu^{2+} in this site. Because Cu^{2+} is smaller by 0.01_5 Å compared to Zn^{2+} (17) and the average Zn–OH spacing is 2.13_5 Å for Zn(1), we estimate the orthorhombic Cu–O spacings to be $a_{x(y)} \approx 2.25$ Å, $a_{y(x)} \approx 2.11$ Å, and $a_z \approx 2.00$ Å.

In contrast, a distinct Jahn–Teller induced energy and distortion contribution is present if Cu^{2+} occupies the Zn(2) site, which is directly reflected by the smaller orbital contributions to the experimental g values $(g = 2.19)$ compared to those calculated $(g = 2.24)$ (Tables 2 and 3). A rough estimation of the additional ground-state splitting and of the radial distortion parameter indicates that the final values of this splitting and of ρ are comparable to the corresponding values for Cu^{2+} in the Zn(1) site. As already stated, the overall distortion of Cu^{2+} on the Zn(1) and Zn(2) sites in phase II-b is rather small compared to other oxidic compounds (15).

Finally, it is interesting to ask what are the relative amounts of Cu^{2+} being distributed over the Zn(1) and

Zn(2) sites in phase II-b (ratio v). From the simulation of the X- and Q-band spectra (Table 2) we were able to deduce a ratio v of about $0.06_5(1_0)$. The preference for the Zn(2) sites, in which the Cu^{2+} ions are energetically stabilized by an additional vibronic Jahn–Teller distortion component, is striking.

Three additional low intensity signals with g values of about 2.19, ≈ 2.1, and 2.06 are observed in the EPR spectra. While the first two weak features (I_1, I_2) seem to be caused by impurities and cannot be assigned, the third one (H*) shows $g\perp$ properties and an interesting concentration dependence (Figs. 4 and 5). With increasing Cu^{2+} concentration it becomes more prominent with respect to the spectra P1 and P2, which vanish below $x \approx 0.6_5$. In the range $0.6_5 > x > 0.4$ the signal at $g = 2.06$ is still weakly observed. Thus we think that it is caused by Cu^{2+} in phase I'. Though Cu^{2+} is incorporated into the latter phase in high concentrations and hence EPR silence is expected as the consequence of extended exchange interactions with J values $\gg h\nu$, some isolated Cu^{2+} polyhedra may still be present.

4. Analysis of the Diffuse Reflectance Spectra

Further insight into the distribution and chemical surrounding of Cu^{2+} in the I, I', and II-b phases comes from the 5 K diffuse reflectance spectra (Fig. 6). The spectrum of a sample with $x = 0.89_5$ in the d–d region is a superposition of at least two bands centered at about 15500 cm^{-1} and 13300 cm^{-1}. The sharp features at 7200, 6300, 5200, and 4500 cm^{-1} are overtone excitations of OH$^-$ and H$_2$O, as indicated by the spectrum of the pure Zn$_5$(OH)$_8$ (NO$_3$)$_2 \cdot$ 2H$_2$O. As follows from the EPR results, the two observed prominent bands cannot be due to Cu^{2+} in the II-b phase because the corresponding transitions are expected at much lower energies, due to the rather small
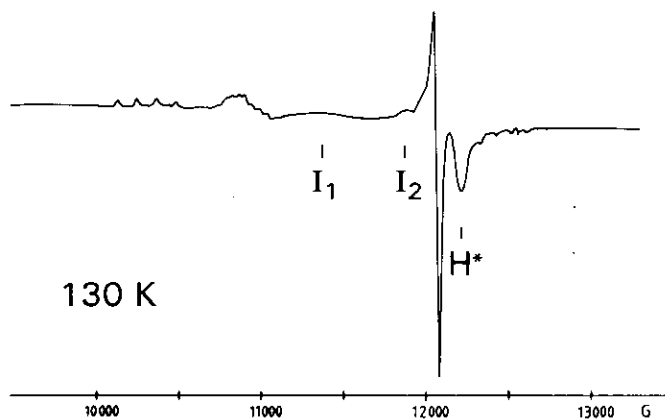

FIG. 5. EPR spectrum (Q-band; 130 K) of a solid Zn$_x$Cu$_{1-x}$(OH)$_{2-y}$ (NO$_3$)$_y \cdot z$H$_2$O with $x = 0.68$. The three features I$_1$, I$_2$, and H* are discussed in the text.
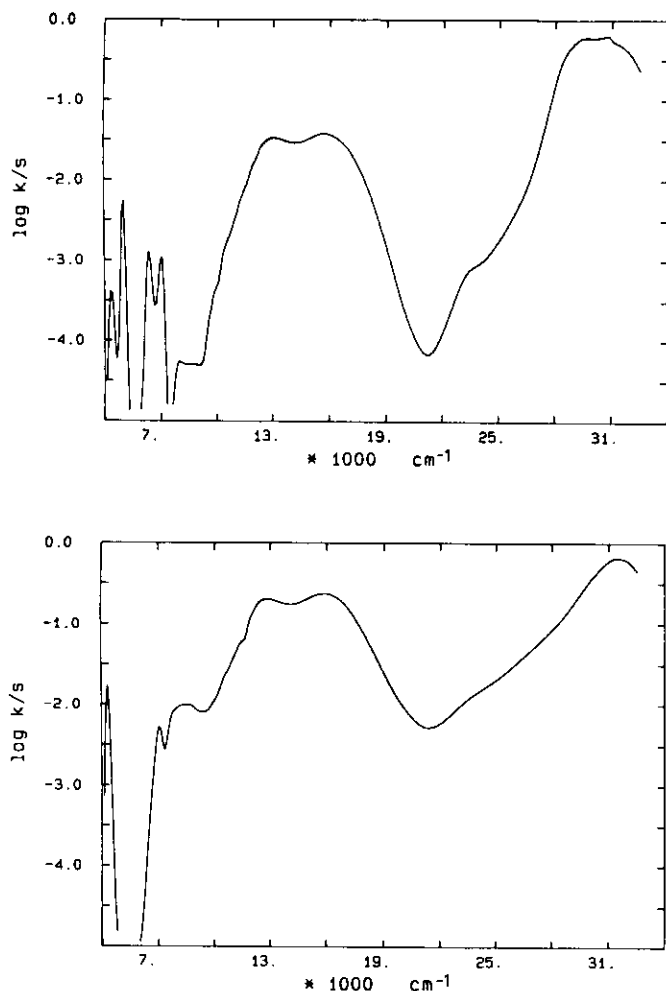
FIG. 6. Ligand field reflectance spectra of compounds Zn_xCu_{1-x} $(OH)_{2-y}(NO_3)_y \cdot zH_2O$ at 5 K in dependence on x [$x = 0.89_5$ (above); $x = 0.57$ (below)].

radial distortion parameters (see Table 3, Zn(1) site). We hence have to assign these bands to Cu^{2+} in the I' phase. At higher Cu^{2+} concentrations down to x values of ≈ 0.55 a third band at 9200 cm^{-1} develops, which—according to the phase diagram in Fig. 1—must also be due to Cu^{2+} in phase I'. The situation closely resembles that observed for mixed crystals $Mg_{2-x}Cu_x(OH)_3NO_3$ (type I structure) (2). While at lower Cu^{2+} concentrations the site allowing a very pronounced Jahn–Teller distortion ($d-d$ transitions between 13000 and 16000 cm^{-1}) is strongly preferred, at higher x values Cu^{2+} is forced to occupy the energetically less favorable site 2 ($d-d$ transitions between 9000 and 13000 cm^{-1}) as well. Similarly one may assume for the Zn^{2+} compounds of type I' that at lower Cu^{2+} concentrations the site Zn(3) in $Zn_3(OH)_4(NO_3)_2$ is preferred by the copper cation, because the *trans* positions of the rather weak oxygen ligator atoms from the NO_3^- anions (Fig. 2)

allow a considerable Jahn–Teller distortion and hence give rise to the higher-energy $d-d$ transitions. In the Zn(1) and Zn(2) ligand geometries the oxygen atoms from NO_3^- occupy *cis* positions and should undergo a less pronounced vibronic distortion. These sites are expected to be preferentially occupied by the Jahn–Teller cation at high Cu^{2+} concentrations and to induce lower energy $d-d$ transitions, as observed. Apparently the ligand field spectra of Cu^{2+} in phases I (either with Zn^{2+} or Mg^{2+} dilution) and I' are very similar, which is not unexpected in view of the structural analogy.

After all, the EPR signal at a g value of about 2.06 (H* in Fig. 5) is most certainly due to Cu^{2+} in the Zn(1) or Zn(2) position of structure I'.

IV. CONCLUSIONS

1. Using structural and spectroscopic methods it was possible to observe three different concentration regions for compounds $(Zn_xCu_{1-x})(OH)_{2-y}(NO_3)_y \cdot zH_2O$, in which limited solid solutions of structural types I, I', and II-b are formed (Fig. 1).

2. Cu^{2+} apparently strongly prefers substitution into phases I and I' rather than replacing Zn^{2+} in phase II-b. This can be understood on the basis of Jahn–Teller coupling because the former phases offer geometrically more flexible host sites with considerably larger distortions and energy stabilizations due to the presence of weak oxygen ligator atoms from the nitrate groups.

3. Cu^{2+} enters phase II-b in only rather small concentrations. Our results clearly demonstrate that both octahedral positions are occupied, with a distinct preference for the Zn(2) site. This result differs from the observation of Stählin and Oswald, who state that Cu^{2+} does not enter phase II-b (10). Finally, we have no evidence for Cu^{2+} substituting Zn(3) in the tetrahedral site.

APPENDIX: EXPRESSIONS FOR THE g (THIRD ORDER CONTRIBUTIONS NOT INCLUDED) AND A VALUES OF Cu^{2+} IN AN ORTHORHOMBICALLY DISTORTED OCTAHEDRAL COORDINATION

Ground State (Metal Contribution)

$$\Psi_g = \cos(\phi/2)d_{x^2-y^2} + \sin(\phi/2)d_{z^2}.$$

g Tensor Components

$$g_z = g_0 + 8\cos^2(\phi/2)u_z$$

$$g_x = g_0 + 2[\cos(\phi/2) + \sqrt{3}\sin(\phi/2)]^2 u_x$$

$$g_y = g_0 + 2[\cos(\phi/2 - \sqrt{3}\sin(\phi/2)]^2 u_y$$

ATANASOV ET AL.

$$u_x = k_x^2 \zeta_0 / \Delta E(^2B_{3g} - {}^2A_g)$$

$$u_y = k_y^2 \zeta_0 / \Delta E(^2B_{2g} - {}^2A_g)$$

$$u_z = k_z^2 \zeta_0 / \Delta E(^2B_{1g} - {}^2A_g).$$

A Tensor Components

$$A_z = P[(-\kappa - 4/7 \cos \phi)\alpha^2 + (1/14)f_1(\phi) \Delta g_y + (1/14)f_2(\phi) \Delta g_x + \Delta g_z]$$

$$A_x = P[(-\kappa + 2/7)(\cos \phi - \sqrt{3} \sin \phi))\alpha^2 + \Delta g_x - (1/14)f_1(\phi) \Delta g_y - (1/7)f_3(\phi) \Delta g_z]$$

$$A_y = P[(-\kappa + (2/7)(\cos \phi + \sqrt{3} \sin \phi))\alpha^2 - (1/14)f_2(\phi) \Delta g_x + \Delta g_y + (1/7)f_3(\phi) \Delta g_z],$$

where short-hand notations have been used as follows:

$$f_1 = (3 + 2\sqrt{3} \sin \phi)/(2 \cos \phi - 1)$$

$$f_2 = (3 - 2\sqrt{3} \sin \phi)/(2 \cos \phi - 1)$$

$$f_3 = (\cos \phi - 1)/\sin \phi.$$

ACKNOWLEDGMENTS

REFERENCES

1. K. Petrov and L. Markov, *J. Mater. Sci.* (1985).
2. M. Atanasov, N. Zotov, C. Friebel, K. Petrov, and D. Reinen, *J. Solid State Chem.* **108,** 37 (1994).
3. G. Kortüm, "Reflexionsspektroskopie." Springer-Verlag, Berlin, 1969.
4. H. Adamsky, "AOMX, a Fortran Computer Package," Institut Theor. Chemie, Universität 40225 Düsseldorf, Germany.
5. C. Friebel, *Z. Naturforsch.* **29B,** 295 (1974).
6. G. Calzaferri and M. Brändle, *QCPE Bull.* **12**(4), (1992); see also G. Calzaferri, L. Forss, and I. Kamber, *J. Phys. Chem.* **93,** 5366 (1989); double zeta functions for Cu^{2+} have been taken from J. W. Richardson, W. C. Nieuwpoort, R. R. Powell, and W. F. Edgel, *J. Chem. Phys.* **36,** 1057 (1962); oxygen $2p$ orbitals were approximated by Slater functions.
7. M. Louër, D. Louër, and D. Grandjean, *Acta Crystallogr. B* **29,** 1696 (1973).
8. H. Effenberger, *Z. Kristallogr.* **165,** 127 (1983).
9. M. Louër and D. Grandjean, *Acta Crystallogr. B* **29,** 1703 (1973).
10. W. Stählin and H. R. Oswald, *Acta Crystallogr. B,* **26,** 860 (1970).
11. B. R. McGarvey, *J. Phys. Chem.* **71,** 51 (1967).
12. A. Abragam and M. H. L. Pryce, *Proc. R. Soc. London A* **230,** 169 (1955).
13. G. Steffen, D. Reinen, H. Stratemeier, M. J. Riley, M. A. Hitchman, H. E. Matthies, K. Recker, F. Wallrafen, and J. R. Niklas, *Inorg. Chem.* **29,** 2123 (1990).
14. J. R. Morton and K. F. Preston, *J. Magn. Reson.* **30,** 577 (1978).
15. D. Reinen and M. Atanasov, *Magn. Reson. Rev.* **15,** 167 (1991).
16. M. J. Riley, M. A. Hitchman, D. Reinen, and G. Steffen, *Inorg. Chem.* **27,** 1924 (1988).
17. R. D. Shannon and C. T. Prewitt, *Acta Crystallogr. B* **25,** 925 (1969).